# Mechanical Properties of Concrete Containing Ferronickel Slag as Fine Aggregate Substitute Using Digital Image Correlation Analysis

Eristra Ernawan, Jessica Sjah, Nuraziz Handika, Sotya Astutiningsih, Eric Vincens

buildings

MDPI

*Article*

# Mechanical Properties of Concrete Containing Ferronickel Slag as Fine Aggregate Substitute Using Digital Image Correlation Analysis

**Eristra Ernawan [1], Jessica Sjah [1,*], Nuraziz Handika [1], Sotya Astutiningsih [2] and Eric Vincens [3]**

[1] Department of Civil Engineering, Faculty of Engineering, Universitas Indonesia, Depok 16424, Indonesia; eristra.nungsatria@ui.ac.id (E.E.); n.handika@ui.ac.id (N.H.)
[2] Department of Metallurgical and Material Engineering, Faculty of Engineering, Universitas Indonesia, Depok 16424, Indonesia; sotya.astutiningsih@ui.ac.id
[3] Univ Lyon, Ecole Centrale de Lyon, CNRS, ENTPE, LTDS, UMR5513, 69134 Ecully, France; eric.vincens@ec-lyon.fr
* Correspondence: jessicasjah@eng.ui.ac.id

**Abstract:** This study aimed to analyze the mechanical, displacement, and strain properties of concrete with Ferronickel Slag (FNS) fine aggregate substitute (0%, 50%, and 100%, by mass, later called FNS-0, FNS-50, and FNS-100, respectively) experimentally using the Digital Image Correlation (DIC) method and the Ultrasonic Pulse Velocity (UPV) test. The FNS used in this study is a by-product that came from a Ferronickel smelter in Indonesia coupled with manufactured sand (M-sand) as the fine aggregate control. A D10 × 20 $cm^3$ cylinder and 15 × 15 × 15 $cm^3$ cube specimens were used to analyze the density, compressive strength, and UPV. Additionally, the cube specimens were tested using the DIC method to analyze the displacement and strain properties. The test results show the highest compressive strength was obtained by FNS-50, followed by FNS-100 and FNS-50. The highest pulse velocity was obtained by FNS-100, followed by FNS-50 and FNS-0. The load–displacement response and strain behavior indicate the specimen that had the most load resistance was FNS-50, followed by FNS-100 and FNS-0. Poisson's ratio obtained using DIC and strain gauges showed consistent results where FNS-0 had the highest values, followed by FNS-50 and FNS-100. Overall, concrete with FNS substitute showed higher density, compressive strength, pulse velocity, and stiffness, as well as lower Poisson's ratio compared to control concrete (FNS-0).

**Keywords:** Digital Image Correlation; Ferronickel Slag; mechanical properties; manufactured sand; Ultrasonic Pulse Velocity

**Citation:** Ernawan, E.; Sjah, J.; Handika, N.; Astutiningsih, S.; Vincens, E. Mechanical Properties of Concrete Containing Ferronickel Slag as Fine Aggregate Substitute Using Digital Image Correlation Analysis. *Buildings* **2023**, *13*, x. https://doi.org/10.3390/xxxxx

Academic Editor(s):

Received: 13 April 2023
Revised: 8 May 2023
Accepted: 30 May 2023
Published: date



## 1. Introduction

The use of industrial by-products has developed in recent years. More alternative by-product materials are used to substitute the use of cement, natural sand, and rocks for concrete to reduce emissions [1] and preserve natural supplies [2]. A concerning problem emerges following the extensive use of natural or river sand for construction purposes where the supplies might not live up to the demand [2]. Suitable industrial by-product replacements for natural sand, such as Granulated Blast Furnace Slag (GBFS) [3], Steel Slag [4], Copper Slag [5,6], and Ferronickel Slag, are considered interesting alternatives to natural sand. Wijaya and Astutiningsih [7] reported that Ferronickel Slag has great potential as an alternative material to natural sand in concrete and mortar with fine aggregates. The use of Ferronickel in industrial segments, such as metallurgy, transportation, military, architecture, construction, electronics, automotive, and more, has been growing over the years. Generally, Ferronickel is used in the production of stainless steel for up to 30% of worldwide production [8]. The battery and metallurgy industry saw a recent increase in

demand for Nickel, which increased the production of Nickel from 2009 to 2022 [9,10]. The United States alone consumes about 220,000 metric tons worth of Nickel. For every one ton of Ferronickel production, around 12–14 tons of Ferronickel Slag (FNS) are produced as a by-product [11]. Indonesia, as the biggest Nickel-producing country in the world, produces 13 million metric tons of Ferronickel Slag each year [12], but this waste is not well used.

A handful of studies have been conducted on the use of Ferronickel Slag (FNS) as mortar and fine aggregate concrete [9,11,13–19]. Previous studies have shown that mortar and concrete containing Ferronickel Slag (FNS) as fine aggregate substitutes have promising properties. Saha and Sarker [14] reported that the use of FNS in Ordinary Portland Cement (OPC) and in Portland Composite Cement (PCC) mortar as a natural sand substitute achieves increased flow workability and 28-day compressive strength with increasing content of FNS until the optimum substitution of 50% FNS. The mortar's compressive strength with FNS substitution above 50% starts to decline, although comparable to the control mortar strength without FNS. In this study, the OPC mortar achieved increased workability and strength up to 18% and 50%, respectively. The PCC mortar (70% OPC and 30% fly ash class F) containing FNS achieved increased flow and strength up to 18% and 45%, respectively. The optimum ratio of FNS results from the best particle packing by the well-graded aggregate combinations, and the improved workability is the result of FNS's relatively larger particle size. Another study by Wijaya [9] showed that PCC mortar containing FNS as a silica sand substitute increased the 28-day compressive strength up to 77% with an optimum substitution of 70% FNS and an additional increase in density up to 15% due to FNS's larger specific gravity. Mustika et al. [15] reported a 55% increase in slump workability but a 17% decrease in 28-day compressive strength in OPC concrete containing 33.3% FNS as a natural sand substitute. A 3.5% increase in density, 6.7% decrease in modulus of elasticity, and 25% decrease in split-tensile strength were also obtained in their research. Edwin et al. [16] studied the effect of FNS as sand replacement in OPC concrete and found that workability increased by 16% in conjunction with an increasing amount of FNS replacement (0–50% replacement) and increased compressive strength up to 10% with an optimum mix of 40% FNS replacement, which provided the lowest porosity in the concrete matrix. The better workability of FNS concrete might be influenced by the lower water absorption and lower surface area of FNS.

Herein, this study aims at analyzing the mechanical behavior of concrete containing FNS fine aggregate using the Digital Image Correlation (DIC) method. A black speckled pattern surface of 15 × 15 × 15 $cm^3$ cubic specimens under compressive load is captured by a camera. The digital images containing the "movement" of pixels, with the help of speckles, based on the initial condition are analyzed through GOM Correlate 2021 software to determine the local displacements under certain loads, which gives access to the load–displacement relationship and its stiffness. Furthermore, the obtained local displacements can be converted into strains and loads into stresses in order to produce the stress–strain relationship and Poisson's ratio. This method proved to be capable and give satisfactory accuracy in measuring the small and large displacement of concrete [20]. Additionally, cylinder specimens are used to measure the 7-, 14-, and 28-day density and compressive strength of concrete, and an Ultrasonic Pulse Velocity (UPV) test is conducted for all specimens before performing the compressive tests.

## 2. Materials and Experimental Program

### *2.1. Materials and Mix Proportions*

The cement used in this study is a typical OPC type I. The FNS fine aggregate is a by-product of a Ferronickel smelter in Indonesia. The FNS made from Nickel ore comes from a smelting and sorting process as a by-product, which is cooled down using water. The water-cooled slag comes out in the form of granules, and granules with a size less than 0.5

mm were used in this experiment. Manufactured sand (M-sand) was used as a more sustainable fine aggregate [21] for the control sample, which is produced in Rumpin, Indonesia. M-sand is made from crushed and granulated mining waste rock. It has a more consistent size distribution than river sand due to a controlled manufacturing process and a smaller surface area, which leads to better concrete performance [22]. The split stone coarse aggregate with a maximum size of 25 mm was obtained from Sudamanik, Indonesia.

Three batches of concrete containing three fine aggregate combinations of FNS and M-sand were made: 0% FNS, 50% FNS, and 100% FNS with percentage by total fine aggregate weight. The properties of aggregates are provided in Tables 1 and 2, and the fine aggregate gradations are provided in Figure 1. Additionally, the composition of the Ferronickel Slag used is provided in Table 3, acquired using X-Ray Fluorescence (XRF) spectrometry on 2 samplings. It was found that the slag is predominantly composed of oxides of $SiO_2$, $Fe_2O_3$, and MgO.

**Table 1.** Fine aggregate properties.

| Properties | 0% FNS | 50% FNS | 100% FNS |
|---|---|---|---|
| Fineness Modulus | 3.17 | 2.72 | 2.73 |
| SSD Specific Gravity | 2.54 | 2.76 | 2.91 |
| Absorption (%) | 1.83 | 1.42 | 0.70 |
| Unit Weight | 1.47 | 1.66 | 1.55 |
| Void (%) | 41.10 | 38.83 | 46.29 |
| Finer Than No. 200 Sieve (%) | 5.80 | 2.80 | 0.90 |

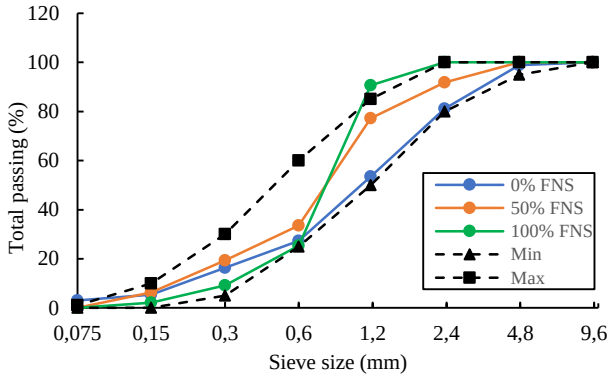


**Figure 1.** Fine aggregates gradations.

**Table 2.** Coarse aggregate properties.

| Properties | Split Stone |
|---|---|
| SSD Specific Gravity | 2.58 |
| Absorption (%) | 1.60 |
| Unit Weight | 1.55 |
| Void (%) | 38.84 |
| Abrasion Loss (%) | 22.23 |

**Table 3.** Ferronickel Slag (FNS) composition.

| Component | Percentage (%) | | |
|---|---|---|---|
| | Sample 1 | Sample 2 | Average |
| $SiO_2$ | 46.98 | 46.84 | 46.91 |
| $Fe_2O_3$ | 14.88 | 15.31 | 15.10 |

| | | | |
|---|---|---|---|
| CaO | 1.39 | 1.45 | 1.42 |
| $Cr_2O_3$ | 1.48 | 1.50 | 1.49 |
| $Al_2O_3$ | 4.13 | 3.94 | 4.04 |
| MnO | 0.51 | 0.52 | 0.52 |
| $P_2O_5$ | 0.46 | 0.49 | 0.48 |
| NiO | 0.08 | 0.09 | 0.09 |
| MgO | 29.39 | 29.17 | 29.28 |
| $SO_3$ | 0.23 | 0.24 | 0.24 |
| $Na_2O$ | 0.00 | 0.00 | 0.00 |
| $TiO_2$ | 0.10 | 0.10 | 0.10 |
| $K_2O$ | 0.00 | 0.00 | 0.00 |

The three combinations of fine aggregate of this study were coded as FNS-0, FNS-50, and FNS-100 for 0% FNS, 50% FNS, and 100% FNS, respectively. The mix proportions for each combination are provided in Table 4.

**Table 4.** Mix proportions.

| Batch | w/c | Water (kg/m$^3$) | OPC (kg/m$^3$) | FNS (kg/m3) | M-Sand (kg/m$^3$) | Split Stone (kg/m$^3$) |
|---|---|---|---|---|---|---|
| FNS-0 | 0.412 | 206 | 501 | 0 | 694 | 992 |
| FNS-50 | 0.412 | 206 | 501 | 347 | 347 | 992 |
| FNS-100 | 0.412 | 206 | 501 | 694 | 0 | 992 |

### *2.2. Specimen Preparations*

#### 2.2.1. Casting and Curing

Each batch of concrete was cast into two types of molds to create two types of specimens, D10 × 20 cm$^3$ cylinders and 15 × 15 × 15 cm$^3$ cubes. The specimens were then compacted using a rod, as ASTM [23] suggests. Then, 24 ± 8 h after casting, the specimens were demolded and cured under water with an average temperature of 22 ± 2 °C for 7, 14, and 28 days for cylinder specimens and 28 days for cubic specimens.

#### 2.2.2. Digital Image Correlation Test Preparations

Cubic specimens were specially treated to facilitate Digital Image Correlation (DIC) analysis. One day before the compressive test, one of the flat surfaces was painted white using wall paint. Afterward, a black speckle pattern was created using spray paint by gently spraying the specimen surface to create bubbly particles that will produce more pronounced and dense black speckles, as shown in Figure 2a,b. Digital images captured by the camera were monochromatic; thus, a white background and black speckles were made to provide a good amount of contrast, which helped the creation of unique subsets and pixel identification for DIC analysis.

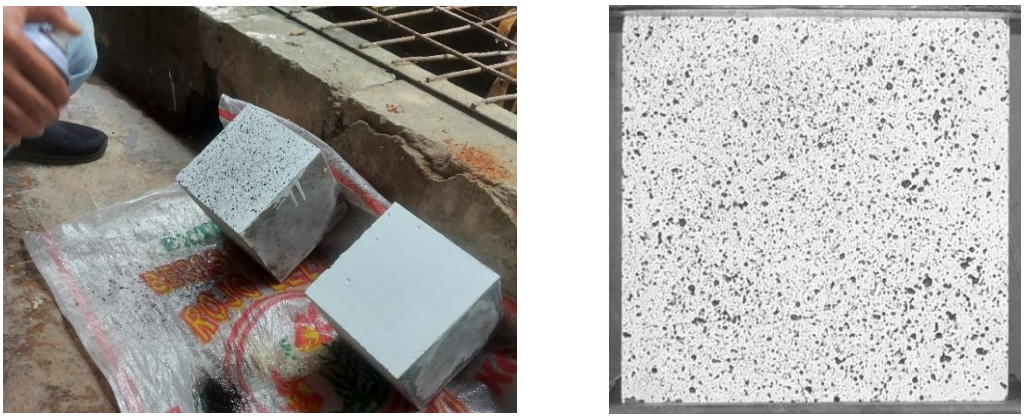

(**a**) (**b**)

**Figure 2.** (**a**) Making of the speckle pattern and (**b**) the result.

Since DIC analysis may have a lower accuracy of strain measurement than interferometric instruments [20,24], an additional source of measurement including two 60 mm strain gauges in both vertical and horizontal directions was applied on the middle of two flat surfaces of each cubic specimen (75 mm from the edges) to measure the vertical and horizontal strains.

### *2.3. Testing Methods*

#### 2.3.1. Ultrasonic Pulse Velocity (UPV) Test

Each cylindrical and cubic specimen was tested using Pundit Lab+ before the compressive strength test was conducted. The UPV test measures the time difference of electromagnetic pulse propagation through an object between two transducers. The two transducers are a pulse transmitter and a pulse receiver. The transmitter emits a 54 kHz electromagnetic pulse through the object and is received by the receiver transducer.

A direct transmission approach was used to measure the velocity of the pulse propagating through the specimens. Two flat directly opposite surfaces of the specimens were smeared with grease. The grease helps to fill the microscopic gap and pores of the concrete so that the transducers can emit the pulses in a uniform way through the specimens. The transducers were then placed on both flat surfaces facing directly to each other. The measurement of travel time and pulse velocity was read three times for each specimen to receive a reasonably small deviation.

#### 2.3.2. Compressive Strength and DIC Test

Cylindrical specimens were tested to measure the 7-, 14-, and 28-day compressive strength according to Indonesian Standard [25] (based on ASTM [26]). Prior to testing, specimens' dimensions and weights were measured to obtain the concrete's densities, which later were capped. These specimens were analyzed to understand the influence of FNS fine aggregate towards concrete's compressive strength and density. The specimens were tested using a hydraulic machine with a maximum load of 1000 kN and loaded under a force-controlled axial load until the specimens reached failure. The failure pattern of each cylinder was analyzed according to ASTM C39-14 typical failure patterns schemes.

The Digital Image Correlation (DIC) method, specifically the 2-dimensional DIC method, is a non-interferometric optical technique that measures the surface deformations of an object. This method is a powerful, flexible, and relatively easy tool since it explicitly provides full-field displacement and strains through the comparison of digital images of the object surface captured by a high-resolution camera before deformations happened (the "reference" image) and after the deformations took place [24]. The way it works is

through coordinate reconstruction of the observed points or speckle pattern on the specimen surface based on parallax data for each deformation of each particular speckle. The changes in coordinates of each speckle are then calculated to obtain the displacement and strain of the speckles [27].

The DIC method used in this study is based on several previous research [28–30]. These studies tried to capture and compute the speckles' movement under compressive or bending load on cylindrical, cubic, and reinforced beam concrete specimens' surface using a digital camera with the help of GOM Correlate 2021 computing software. They succeed in computing the speckles' movement and converting it into displacement and strain fields.

The DIC test was carried out parallel with the 28-day compressive strength test along with the strain gauge reading of cubic specimens. A Fujifilm X-A3 camera attached to a tripod was prepared alongside two lighting devices placed on the right side and left side of the camera, as presented in Figure 3. A tripod and a remote shutter were used to ensure the camera's steadiness during the test to minimize vibrations and movements of images, which may sensitively cause miscalculations of the displacement of speckles [28]. The two lightings were used to aid the camera's focus, as well as to ease the software analysis with brighter and more crisp images. Additionally, a clock was placed in front of the camera without blocking the specimen's surface to provide a way to connect the strain gauges to time. The cube specimen was placed in the test machine with the speckled surface facing the camera. The camera was positioned in such a way as to be perpendicular to the specimen's speckled surface and set to be at the same height as the specimen's centroid. The installed strain gauges on the specimen's surfaces were connected to a National Instruments (NI) processing device using the lead wires attached to the strain gauges. The measurement of the strain gauges was read using LabVIEW National Instrument software 2011. The cubes' compressive strength test method and machine are identical to the cylindrical specimens. Throughout the compressive test, the camera starts to capture three frames per second (3 fps) before the load is applied to the specimen until failure.

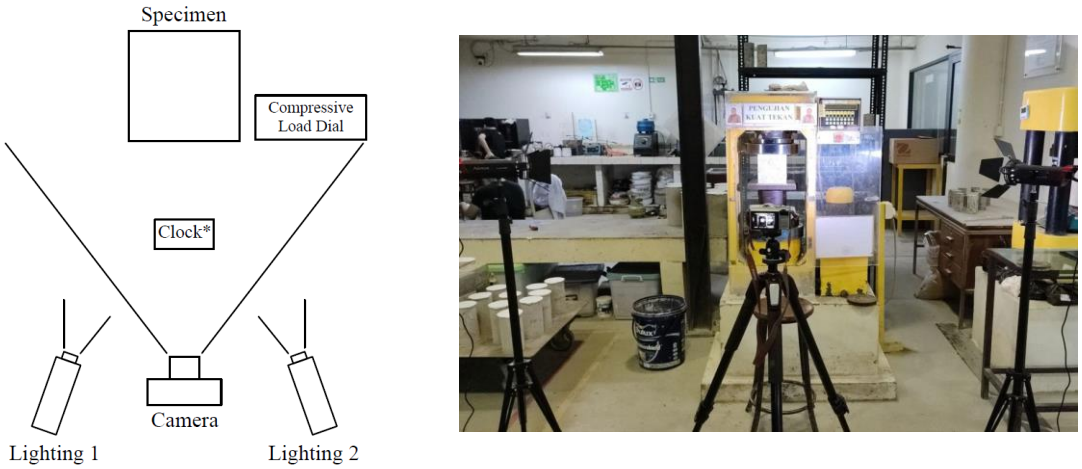


**Figure 3.** (**a**) The DIC test scheme (* Clock positioned without blocking the specimen) and (**b**) setup.

The captured digital images were then analyzed through GOM Correlate 2021 software. The software measures the displacement and strain field of the speckled surface in reference to the image right before the load dial starts to read (the "reference image"). Figure 4 shows nine observation points that were determined on the speckled surface to provide displacement and strain magnitudes. The load readings across all images were captured and inputted manually to provide a relationship between load readings and displacements, as well as strains produced by the software. In addition, strain measurements

from the strain gauges were matched with the clock's time captured in the images to provide additional strain measurements.


**Figure 4.** Observation points.

## 3. Results and Discussion

### *3.1. Density*

The results for the 7-, 14-, and 28-day density measurements of every batch are provided in Table 5 and Figure 5, with each value representing the average density of four samples for each type of specimen. Based on the results acquired, the density of all specimens ranged from 2.28 to 2.42 g/cm$^3$. The highest density of 2.42 g/cm$^3$ was found in 28-day FNS-50 cylinder specimens with a 3.4% increase, and the lowest density of 2.28 g/cm$^3$ was found in FNS-0 specimens. Although the highest density was found in the FNS-50 batch, the overall density of FNS-50 across almost all ages and specimen types was lower than that of FNS-100. The densities of the FNS-50 and FNS-100 batches were slightly higher than that of FNS-0. These results aligned with the aggregate's specific gravity, where the case of 100% FNS substitution led to the highest density, followed by the case of 50% and the 0% FNS substitutions. The use of FNS in concrete tends to marginally increase the concrete's density based on the amount of substitution due to the higher specific gravity and unit weight. However, the results of the control batch (FNS-0) were a fraction lower than the normal concrete density of approximately 2.35–2.45 g/cm$^3$. These results occurred due to the usage of manufactured sand (M-sand), which has a slightly lower specific gravity than natural sand (2.6–2.8 g/cm$^3$). Hence, FNS substitutions in concrete did not significantly affect the concrete's density.

**Table 5.** Results for density.

| Batch | Specimen | Density (g/cm$^3$) | | |
|---|---|---|---|---|
| | | 7 d | 14 d | 28 d |
| FNS-0 | Cylinder | 2.28 (-) * | 2.28 (-) | 2.34 (-) |
| | Cube | - | - | 2.28 (-) |
| FNS-50 | Cylinder | 2.32 (+1.7%) | 2.35 (+3.3%) | 2.42 (+3.4%) |
| | Cube | - | - | 2.35 (+3.2%) |
| FNS-100 | Cylinder | 2.38 (+4.0%) | 2.40 (+5.2%) | 2.39 (+2.3%) |
| | Cube | - | - | 2.35 (+3.2%) |

* Note: Values inside the parentheses are relative values with respect to the FNS-0 case (control specimen) with its specimen type and age counterpart, and a positive sign indicates an increase.

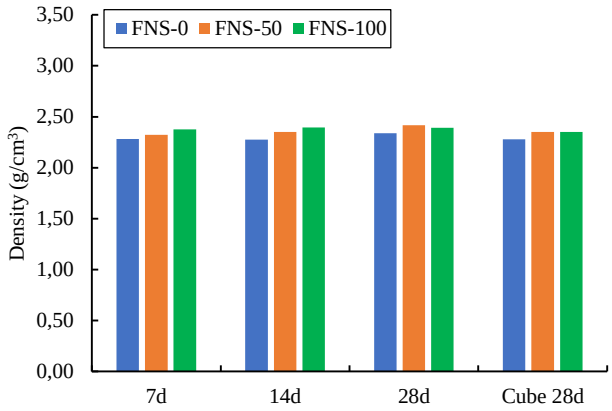


**Figure 5.** Effects of FNS substitution on density.

### *3.2. Compressive Strength*

Due to the effect of the specimen's shape, the D10 × 20 cm³ cylindrical specimens and 15 × 15 × 15 cm³ cubic specimens' compressive strength were converted into D15 × 30 cm³ cylindrical compressive strength (fc') based on the conversion guidance in the French standard CERIB 46-E. The converted compressive strength test results are shown in Figure 6, which provides an image of the effect of FNS substitution. It can be seen that partial and full FNS substitution increases 7-, 14-, and 28-day cylinder compressive strength. The lines' slope between batches indicates the changes in compressive strength for each batch per respective age. Table 6 shows the effect of the addition of FNS in the sample. It increases the 7-day compressive strength of FNS-100 up to 15.2% (32.0 MPa) and of FNS-50 up to 9.1% (30.3 MPa) compared to FNS-0 (27.8 MPa). The 7-day strength of FNS-100 seems to be the highest among the others. Though several studies [9,13,15,16] did not report any higher early strength of concrete containing 100% FNS substitution, further study may be carried out to analyze the possibility of FNS influence on early strength development. The 14-day compressive strength of FNS-50 was found to be the highest, followed by FNS-100 and FNS-0 with 32.6 MPa, 31.8 MPa, and 29.6 MPa, respectively. The strength improvements were 10.1% and 7.6% for FNS-50 and FNS-100, respectively compared to FNS-0. Furthermore, FNS-50 led to the highest 28-day compressive strength followed by FNS-100 with 41.4 MPa and 37.0 MPa, respectively, which were 21.1% and 8% greater than FNS-0 (34.2 MPa), respectively. The failure pattern of cylinders across all batches and specimens was similar to a Type III vertical cracking failure pattern with no well-formed cones based on ASTM C39-14, except FNS-50 at 28 days old with a Type II vertical crack with well-formed cones.

**Table 6.** Results for compressive strength, fc'.

| Batch | Specimen | Density (g/cm³) | | |
|---|---|---|---|---|
| | | 7 d | 14 d | 28 d |
| FNS-0 | Cylinder | 27.8 (-) * | 29.6 (-) | 34.2 (-) |
| | Cube | - | - | 35.5 (-) |
| FNS-50 | Cylinder | 30.3 (+9.1%) | 32.6 (+10.1%) | 41.4 (+21.1%) |
| | Cube | - | - | 40.2 (+13.2%) |
| FNS-100 | Cylinder | 32.0 (+15.2%) | 31.8 (+7.6%) | 37.0 (+8.0%) |
| | Cube | - | - | 40.1 (+12.8%) |

* Note: Values inside the parentheses are relative values with respect to the FNS-0 case (control specimen) with its specimen type and age counterpart, and a positive sign indicates an increase.

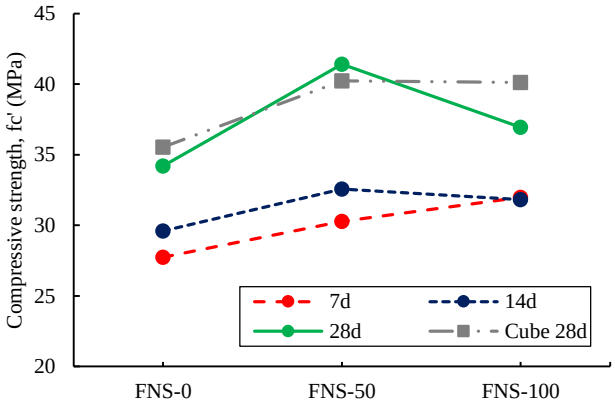


**Figure 6.** Effects of FNS substitution on compressive strength.

The cube specimen compressive strengths obtained during tests were compromised. The values of FNS-50 and FNS-100 cube strength could not be obtained, supposedly due to test machine limitations. The values in Table 6 could be achieved higher since the majority of FNS-50 and all FNS-100 cube specimens did not fail under 1000 kN compressive load, and therefore the tests had to be stopped earlier. As a consequence of the matter, only the captured behavior of the affected specimens was analyzed. Despite the compromised results, the effect of FNS substitution remains the same as the cylinder specimens, where FNS substitution yields a higher compressive strength of 40.24 MPa and 40.11 MPa in FNS-50 and FNS-100, respectively, than FNS-0 (35.54 MPa). The strength increase was 13.2% and 12.8% for FNS-50 and FNS-100 specimens, respectively.

The obtained strength results in this study slightly differ from previous studies of FNS concrete. Saha and Sarker [13] found a decrease in compressive strength in 100% FNS replacement of natural sand, although their particular 100% FNS' fineness modulus was generally lower. They explained this feature by the fact that the particle size distribution with the substitutive led to a less compact granular structure than that of the control specimen (FNS-0), leading to a smaller strength. In this study, the final grading in FNS-100 seems to not induce a looser granular structure than that of the control specimen (FNS-0). Furthermore, Edwin et al. [16] reported an enhancement of strength up to 50% FNS replacement due to the Ferronickel Slag's particle shape. Its sharp angular edges and rough surface improved the cohesion and slip resistance between aggregate and paste. However, their 50% FNS concrete did not perform well compared to this study with a minor strength improvement of around 2% than that of the control specimen. A possible explanation lies in bigger particle sizes than in the case of natural sand and in a greater void ratio, which might provide a worse strength performance than with natural sand. However, the FNS used in this study had generally larger particle sizes and a higher void ratio in the case of 100% replacement and had a better strength than that of the control specimens (FNS-0). The particle size distribution of FNS might play a more significant role in affecting the strength performance, which explains the contradictory results across these studies. Further study of the FNS particle size distribution effect on concrete strength must be considered in the future.

### *3.3. Ultrasonic Pulse Velocity*

The measurement of UPV for every specimen was collected and plotted in a box and whisker (Figure 7) to provide an image of UPV data distribution. It shows that the cylinder data variance of UPV is largest at 7 days, larger at 14 days, and smallest at 28 days. The cube data variance shows a wider-ranged distribution, especially the FNS-50 batch, with a minimum–maximum extrema and first–third quartile range between 4.54–4.79 km/s and 4.56–4.78 km/s, respectively. Fortunately, no outliers were obtained between these widespread data. The lower boxes represent the first quartile and median, whereas the upper

boxes represent the median and third quartile. The whiskers or lines below and above the boxes represent the "error bars" or the difference in the minimum and maximum values of data to the first and third quartiles, respectively.

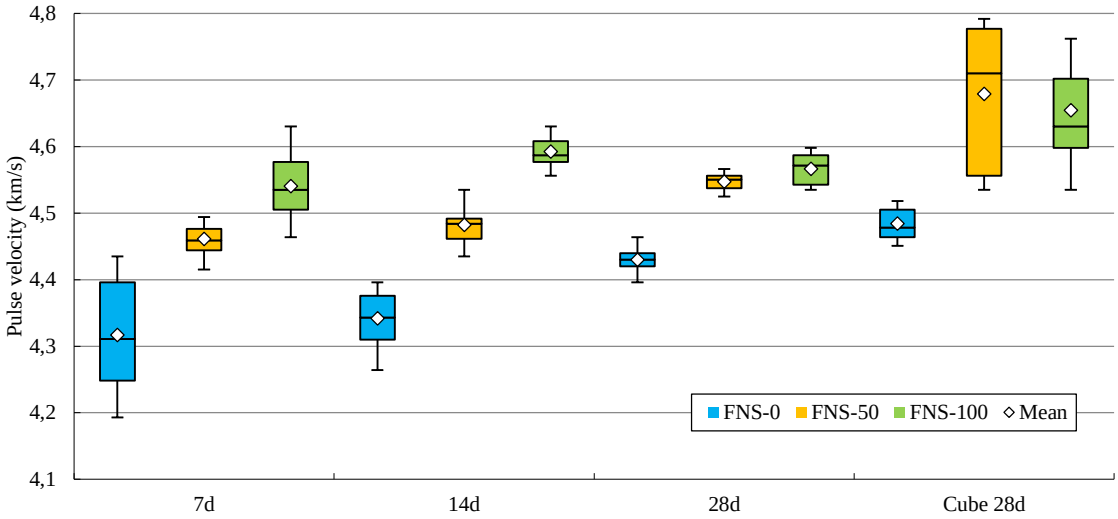


**Figure 7.** Ultrasonic Pulse Velocity data distribution in box and whisker.

The unconverted compressive strengths previously obtained were plotted against UPV to provide a relationship between compressive strength and UPV. Figure 8 shows an exponential correlation between compressive strength and UPV, as given by Equation (1)

$$y = 0.43e^{0.97x} \quad (1)$$

where $y$ is the compressive strength (MPa), and $x$ is the pulse velocity (km/s) with a coefficient of correlation, $R^2$, of 0.70. It can be seen that a lower-strength specimen tends to have a lower velocity. A slower wave propagation gives a less hardened concrete and thus a lower compressive strength [31]. However, the FNS-100 cylinder specimens tend to have the highest pulse velocity, although their compressive strengths were lower than FNS-50 at ages 14 and 28 days. This behavior is considered to be an anomaly since, generally, study results have stated a positive correlation between Ultrasonic Pulse Velocity and compressive strength [31–34].

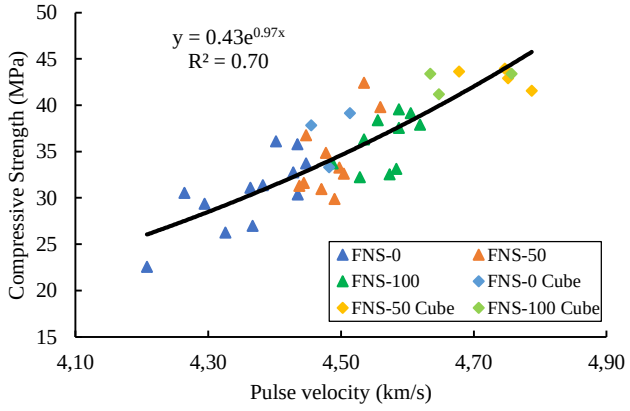


**Figure 8.** Relationship between compressive strength and pulse velocity.

An increase in velocity might be influenced by the oxide compositions contained in FNS, as it is high in magnesium and iron oxides [9,11,17,18]. Following the matter, further

study regarding the effect of oxide compositions of FNS on UPV may be carried out to understand the aforementioned higher pulse velocity.

### *3.4. Load–Displacement Relationship*

Post-processed images through GOM Correlate 2021 were then plotted against compressive load to create a load–displacement relationship. Figure 9 shows the displacement in the $y$-direction of one representative specimen from each batch, later called vertical displacement or $v$-displacement, against the applied load. Figure 10 shows the $v$-displacement field of the specimens. All variations seemed to have a relatively constant response at early loading or elastic phase for every observation point.

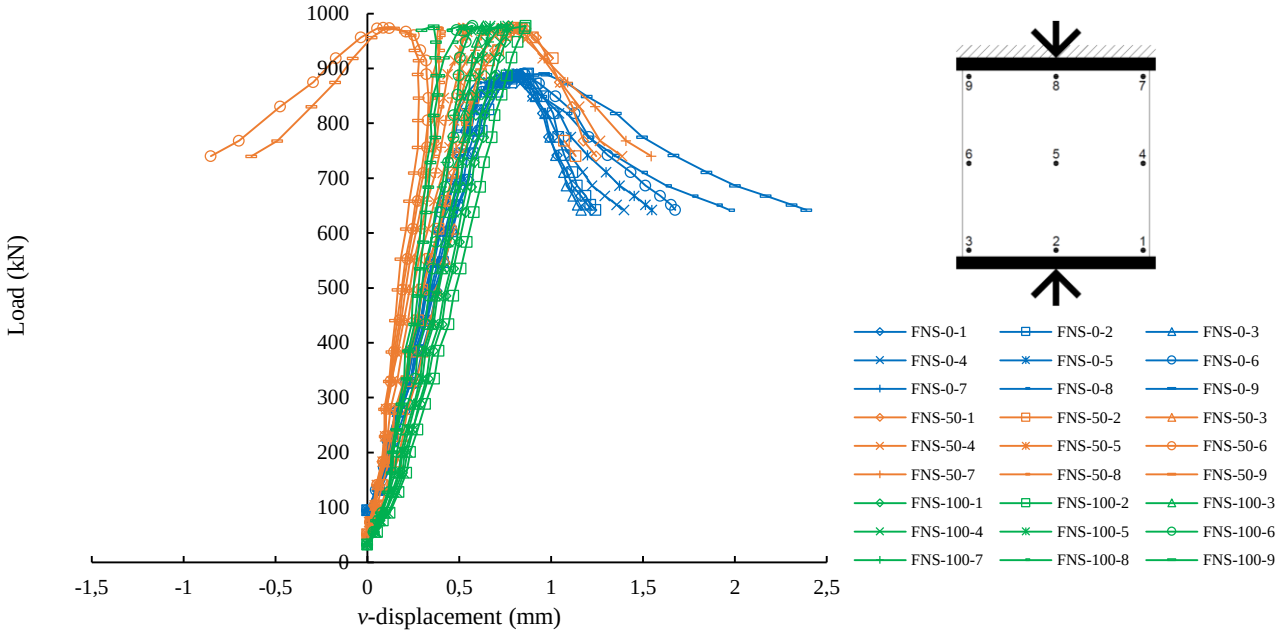


**Figure 9.** Load–displacement response of cubic specimens.

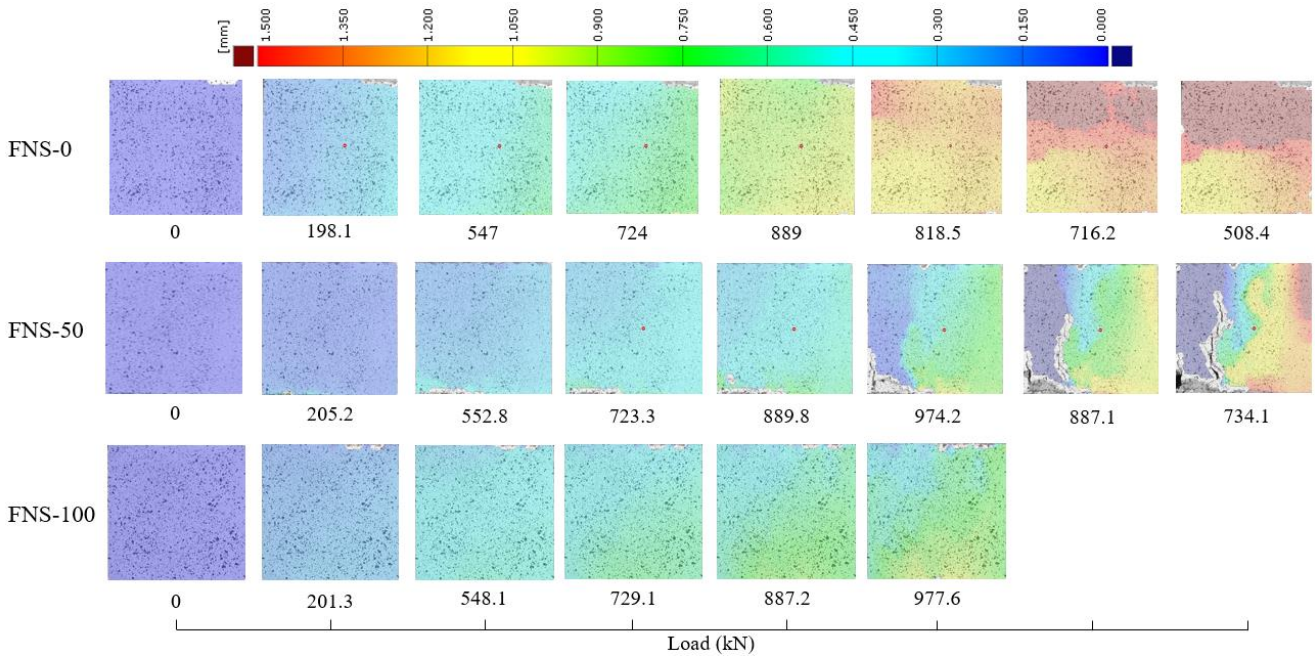


**Figure 10.** $v$-displacement field of cubic specimens.

FNS-0 specimen's displacement field for all observation points was increasing linearly upward (positive *y*-direction) until the maximum load was reached before a softening phase. Prior to the maximum load, the displacement response of FNS-0 observation points started to differ from the normal condition. When the load reached the 724–889 kN mark, the lower right part of the specimen, Points 1, 2, and 4, gained a noticeably larger displacement (Figure 10). The average *v*-displacement of all FNS-0 observation points when they reached the maximum load was 0.935 mm. In subsequent images, in the upper part of the specimen, Points 7–9, a much larger displacement occurred than in the lower part (Points 1–3). A divided upper and lower part may indicate a horizontal crack that appears at the mid-height of the specimen.

One of the FNS-50 specimens reached failure and was used as a representative specimen. The FNS-50 specimen's displacements for all observation points increased linearly upward until the maximum load reached before a softening phase. From the start, the displacement of all observation points moved uniformly before reaching the maximum load (Figure 10). The average *v*-displacement of all FNS-0 observation points when they reached the maximum load was 0.531 mm. At the 974.2 kN mark, the specimen started to show two distinct *v*-displacement fields, the left (Points 3, 6, and 9) and the right part (Points 1–2, 4–5, and 7–8) of the specimen. The left part shows a lower displacement (tends to decrease), and the right part shows a higher displacement (tends to increase). This behavior indicates a vertical deformation happened between these two parts, which later can be seen in Figure 11. Noticeable cracks occurred at the 974.2–734.1 kN mark, where the area around Point 1 was already deformed, and a vertical crack between the left and right parts developed during this period. Additionally, Points 6 and 9 started to decrease and moved downward (negative values) after they reached the maximum load.

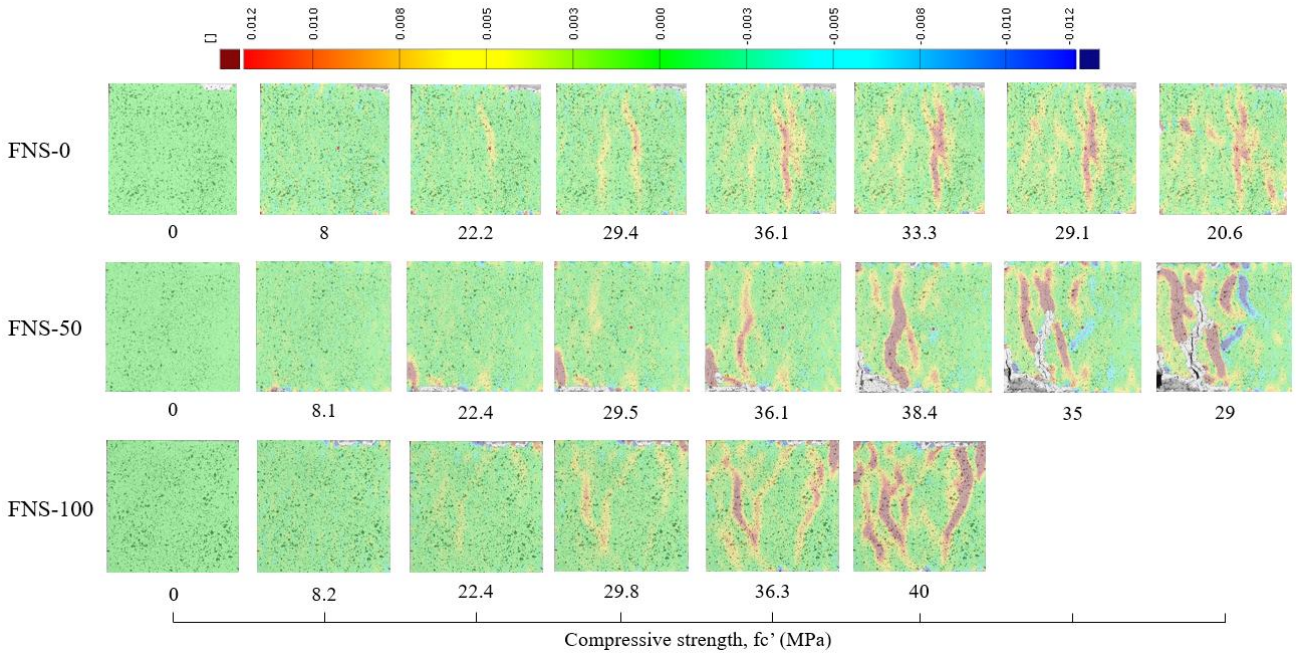


**Figure 11.** *xx*-strain field of cubic specimens.

As previously mentioned, all FNS-100 specimens did not reach their failure, and therefore only the captured response was analyzed due to testing machine limitations. The FNS-100 specimen's displacement for all observation points increased linearly upward until the load reached 844.7 kN. Prior to reaching the maximum load of 977.6 kN, the FNS-100 specimen entered the semi-plastic or transition phase with evidence of the non-linear response initiation in all observation points (Figure 10). Figure 10 shows the development of FNS-100's non-linear response when the load reached 729.1–887.2 kN,

where the lower right part of the specimen (Points 1, 2, and 4) gained a larger displacement. It later can be seen that at 977.6 kN, the displacement of Points 1, 2, 3, and 4 grew larger than the other points. The average $v$-displacement of all FNS-100 observation points when they reached the maximum load was 0.67 mm.

Based on the load–displacement relationship diagram, the FNS-100 seemed to have a higher resistance than FNS-50, though the latter average strength was higher than the former, which is represented by a steeper response in the load–displacement relationship graph (Figure 9). Compared to FNS-0, both FNS-50 and FNS-100 show a lower displacement response or higher resistance due to the steeper response of the load–displacement relationship.

### *3.5. Strain Behavior*

The post-processed images also gave us the $xx$-strains or horizontal strains to analyze the vertical crack patterns that occurred on the specimens. Figure 11 provides the $xx$-strain field development of the representative cube specimens of each batch against their respective compressive stress. The shown specimens are identical to the previous load–displacement diagram.

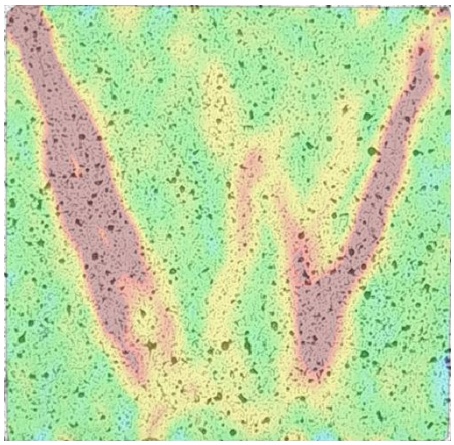

**Figure 12.** Inclined cracks on an FNS-100 specimen under 38.1 MPa load (equal strain scale as in Figure 11).

The FNS-0 specimen's strain field signifies multiple columnar soft cracks, identified by the yellow (≥0.005) and red (≥0.010) strain area that appear from the 29.4 MPa mark until later images (Figure 11). Although the strain field has no physical meaning, it can be used to indicate the crack location due to the localization of crack displacement [29].

The FNS-50 specimen's strain field shows an early emerging large deformation (strain ≥ 0.010) happening in the lower left part of the specimen (Point 3), which appears at the 22.4 MPa mark (Figure 11). Additionally, multiple columnar cracks start to appear at the 36.1–38.4 MPa mark, shown by the yellow (≥0.005) and red (≥0.010) strain field. The large vertical strain that occurs in the 38.4 MPa image explains the occurrence of two divided parts of displacement fields mentioned earlier (Figure 10). Other than the large vertical strain, the lower left part is largely deformed, and the slightly inclined cracks are also starting to develop. These developing cracks are more visible (strain ≥ 0.010) in later images (past the maximum stress), adjacent to the growing vertical crack opening.

The FNS-100 specimen has the most interesting crack pattern development than the other ones. The crack propagation started to emerge at 29.8 MPa based on the yellow (≥0.005) and red (≥0.010) strain area, which forms multiple columnar cracks. These cracks started to grow and formed some mildly inclined cracks in later stages. The inclined cracks may indicate an influence of shear stress. This evidence is more pronounced on another FNS-100 specimen's surface (Figure 12) where it shows two major inclined columnar

cracks forming a "V" shape under 38.1 MPa load. Therefore, concrete with fully substituted fine aggregate using FNS may produce a larger shear stress than in the case of normal concrete. Further studies are required to better analyze the effect of FNS fine aggregate on shear failure under compression. Compared to FNS-0, the cracks that appeared in FNS-100 seem more apparent, although the working load was relatively larger. However, compared to FNS-50, no visible crack openings appeared in FNS-100, which indicates a better resistance for this particular specimen.

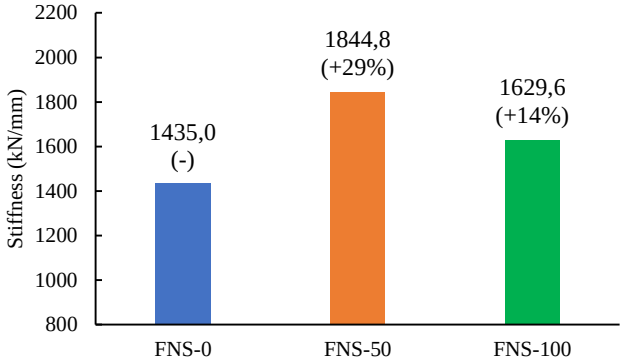


**Figure 13.** Effect of FNS substitution on stiffness.

### *3.6. Stiffness*

The stiffness of concrete was calculated using the load–displacement response in Figure 9. Stiffness values calculated based on the slope of linear region of the vertical load–displacement graph, where the elastic phase of the concrete is represented by Equation (2)

$$Stiffness = \frac{\Delta F}{\Delta l} \quad (2)$$

where $\Delta F$ is the change in compression force applied to the specimen, and $\Delta l$ is the change in vertical displacement of Point 5 based on the reference image. The $v$-displacement of Point 5 was similar (relatively little deviation) to the average displacement of every point, so it could represent and was used to calculate the specimen's stiffness.

The obtained average stiffness values of each batch are provided in Figure 13. The stiffness values of FNS-0, FNS-50, and FNS-100 were 1435 kN/mm, 1844.8 kN/mm, and 1629.6 kN/mm, respectively. The stiffness improvements were 29% and 14% for FNS-50 and FNS-100, respectively, compared to FNS-0. It can be seen that FNS-50 has the highest stiffness, followed by FNS-100 and FNS-0. The higher values are represented by the steeper slope in Figure 9. These results indicate that the partially substituted FNS concrete had the highest load resistance and thus portrayed the compressive strength results, where FNS-50 had the overall highest ultimate strength, followed by FNS-100 and FNS-0. The usage of FNS seems to reduce the deformation of concrete by up to 50% of substitution and decline at 100% substitution. Regardless, the concrete containing FNS had lower vertical displacement than the concrete without FNS.

### *3.7. Poisson's Ratio*

Poisson's ratio values of each batch were obtained using the slope of $xx$-strain vs. $yy$-strain relationship (lateral vs. longitudinal strains) in the linear region or up to 30% of the specimen's ultimate strength [35]. This relationship was gathered from the DIC analysis (using Point 5) and strain gauge measurement.

The results for Poisson's ratio are provided in Table 7. It provides the results calculated from the DIC and strain gauge for every batch. Poisson's ratios calculated using DIC analysis were 0.24, 0.22, and 0.22 for FNS-0, FNS-50, and FNS-100, respectively. The values calculated using the strain gauge were 0.27, 0.22, and 0.20 for FNS-0, FNS-50, and FNS-

100, respectively. These values are still considered to be in the range of the usual concrete's Poisson's ratio of 0.10–0.30 [35,36]. Based on the results shown, a higher FNS substitution yields a lower Poisson's ratio. It can be seen, representatively, according to Belyadi et al. [37], that a higher Poisson's ratio implies that one specimen is able to withstand fracture better than the lower ones. However, the highest Poisson's ratio in FNS-0 produced a lower compressive strength than other batches. According to Park and Paulay [36], generally, a higher-strength concrete has a relatively lower Poisson's ratio. This statement crudely explains why the lower Poisson's ratio in FNS-50 and FNS-100 yielded a higher compressive strength than FNS-0.

**Table 7.** Poisson's ratio results.

| Batch | Poisson's Ratio | |
|---|---|---|
| | DIC | Strain Gauge |
| FNS-0 | 0.24 | 0.27 |
| FNS-50 | 0.22 | 0.22 |
| FNS-100 | 0.22 | 0.20 |

## 4. Conclusions

The mechanical response of concrete containing Ferronickel Slag (FNS) fine aggregate was analyzed using the compressive strength test and the Digital Image Correlation (DIC) method. FNS was used as a fine aggregate substitute with manufactured sand (M-sand) as the concrete's control aggregate (FNS-0). The experimental results such as density, compressive strength, Ultrasonic Pulse Velocity (UPV), vertical load–displacement response, lateral strain behavior, stiffness, and Poisson's ratio were discussed. Based on the results obtained, the following conclusions can be summarized as below:

- The usage of FNS as fine aggregate slightly increases the density of concrete. The density increases scales with the increase in FNS replacement. The 50% and 100% FNS replacements increase the density up to 3.4% and 5.2%, respectively;
- The overall compressive strength of specimens with 50% FNS substitution (FNS-50) has the highest values, followed by 100% FNS substitution (FNS-100) and the control (FNS-0). The 50% and 100% FNS substitutions improve compressive strength up to 21% and 15%, respectively, compared to that obtained for the control specimen (FNS-0). These results show that FNS substitution positively impacts the concrete's compressive strength;
- Ultrasonic Pulse Velocity (UPV) test results show an increase in pulse velocity with an increase in FNS substitution. The UPV data distribution in cylinder specimens shows a tighter range than the cube specimens. The highest velocity achieved by FNS-100 differs from other studies, where it shows a lower compressive strength than FNS-50. Generally, higher pulse velocity leads to a higher strength. These findings may be influenced by magnesium and iron oxides in FNS, which increase the pulse velocity obtained;
- The load–displacement relationship shows the vertical displacement behavior of the specimen behavior under compressive load. The specimen with FNS substitution shows less displacement under the same load compared to the control, where FNS-50 has the steeper response, followed by FNS-100 and FNS-0;
- The stress–strain diagram exhibits the crack patterns of cubic specimens. The FNS-100 specimen has the most interesting crack propagation in which it has a significant influence on the working shear stress, with the result of inclined cracks on the specimen's surface. In some ways, full FNS substitution produces larger shear-stress-induced cracks than the others. On the contrary, the 50% FNS substitution did not show any major damage on the surface. Additionally, sufficient vertical cracks occurred in the FNS-0 specimen;

- The stiffness of FNS substituted specimens leads to higher values than that for the control specimen. The results show that the 50% and 100% FNS substitution increases the stiffness up to 19% and 5%, respectively. It shows that concrete with FNS has a higher load resistance;
- Poisson's ratio values obtained herein show a decrease with an increase in FNS replacement. The results show consistent values between the two methods of measurements, DIC and strain gauge, where full FNS concrete produces the lowest Poisson's ratio, followed by 50% substitution and the control specimen (0% substitution);
- The utilization of Ferronickel Slag fine aggregate in concrete can be an alternative to concrete's fine aggregate since it shows relatively better mechanical properties than that of usual concrete;
- Further study may be carried out to analyze the effect of FNS against early compressive strength and Ultrasonic Pulse Velocity, as well as the effect of the particle size distribution of FNS against compressive strength.

**Author Contributions:** Conceptualization, E.E., J.S., and N.H.; methodology, E.E., J.S., and N.H.; software, E.E.; validation, J.S. and N.H.; formal analysis, E.E.; investigation, E.E.; resources, E.E. and S.A.; data curation, E.E., J.S., and N.H.; writing—original draft preparation, E.E.; writing—review and editing, E.E., J.S., N.H., and E.V.; visualization, E.E.; supervision, J.S. and N.H.; project administration, E.E.; funding acquisition, J.S., S.A., and N.H. All authors have read and agreed to the published version of the manuscript.

**Funding:** This research was funded by the Directorate of Research and Development, Universitas Indonesia, under Hibah PUTI 2022 (Grant No. NKB-1476/UN2.RST/HKP.05.00/2022).

**Data Availability Statement:** The data presented in this study are available on request from the corresponding author.

**Acknowledgments:** The authors wish to thank PT. Jaya Beton Indonesia for providing the materials used in this study.

**Conflicts of Interest:** The authors declare no conflicts of interest.

## References

1. Scrivener, K.L. Options for the Future of Cement. *Indian Concr. J.* **2014**, *88*, 11–21.
2. Sankh, A.C.; Biradar, P.M.; Naghathan, S.J. Recent Trends in Replacement of Natural Sand with Different Alternatives. *IOSR J. Mech. Civ. Eng.* **2014**, *ICAET 1*, 59–66.
3. Patra, R.K.; Mukharjee, B.B. Influence of Incorporation of Granulated Blast Furnace Slag as Replacement of Fine Aggregate on Properties of Concrete. *J. Clean. Prod.* **2017**, *165*, 468–476. https://doi.org/10.1016/j.jclepro.2017.07.125.
4. Dong, Q.; Wang, G.; Chen, X.; Tan, J.; Gu, X. Recycling of Steel Slag Aggregate in Portland Cement Concrete: An Overview. *J. Clean. Prod.* **2021**, *282*, 124447. https://doi.org/10.1016/j.jclepro.2020.124447.
5. Prithiviraj, C.; Swaminathan, P.; Kumar, D.R.; Murali, G.; Vatin, N.I. Fresh and Hardened Properties of Self-Compacting Concrete Comprising a Copper Slag. *Buildings* **2022**, *12*, 965. https://doi.org/10.3390/buildings12070965.
6. Rohini, I.; Padmapriya, R. Properties of Bacterial Copper Slag Concrete. *Buildings* **2023**, *13*, 290. https://doi.org/10.3390/buildings13020290.
7. Wijaya, R.; Astutiningsih, S. Studi Literatur Potensi Pemanfaatan Terak Nikel (Slag Nikel) sebagai Agregat pada Mortar dan Beton. *Bentang* **2021**, *9*, 93–100. https://doi.org/10.33558/bentang.v9i2.2862.
8. Johnson, J.; Reck, B.K.; Wang, T.; Graedel, T.E. The Energy Benefit of Stainless Steel Recycling. *Energy Policy* **2008**, *36*, 181–192. https://doi.org/10.1016/j.enpol.2007.08.028.
9. Wijaya, R. Karakteristik Dan Kuat Tekan Mortar Dengan Subtitusi Terak Nikel Sebagai Agregat Halus. Master's Thesis, Universitas Indonesia, Depok, Indonesia, 2021.
10. U.S. Geological Survey, 2023. *Mineral Commodity Summaries 2023*. https://doi.org/10.3133/mcs2023.
11. Saha, A.K.; Sarker, P.K. Expansion Due to Alkali-Silica Reaction of Ferronickel Slag Fine Aggregate in OPC and Blended Cement Mortars. *Constr. Build. Mater.* **2016**, *123*, 135–142. https://doi.org/10.1016/j.conbuildmat.2016.06.144.
12. Kemenperin Angkat Potensi Slag Nikel Jadi Bahan Baku Industri. 2020. Available online: https://kemenperin.go.id/artikel/21806/Kemenperin-Angkat-Potensi-Slag-Nikel-Jadi-Bahan-Baku-Industri (accessed on 15 May 2021).
13. Saha, A.K.; Sarker, P.K. Sustainable Use of Ferronickel Slag Fine Aggregate and Fly Ash in Structural Concrete: Mechanical Properties and Leaching Study. *J. Clean. Prod.* **2017**, *162*, 438–448. https://doi.org/10.1016/j.jclepro.2017.06.035.

14. Saha, A.K.; Sarker, P.K. Compressive Strength of Mortar Containing Ferronickel Slag as Replacement of Natural Sand. *Procedia Eng.* **2017**, *171*, 689–694. https://doi.org/10.1016/j.proeng.2017.01.410.
15. Mustika, W.; Salain, I.M.A.K.; Sudarsana, I.K. Penggunaan Terak Nikel Sebagai Agregat Dalam Campuran Beton. *Spektran* **2016**, *4*, 36–45. https://doi.org/10.24843/SPEKTRAN.2016.v04.i02.p05.
16. Edwin, R.S.; Ngii, E.; Talanipa, R.; Masud, F.; Sriyani, R. Effect of Nickel Slag as a Sand Replacement in Strength and Workability of Concrete. *IOP Conf. Ser. Mater. Sci. Eng.* **2019**, *615*, 012014. https://doi.org/10.1088/1757-899X/615/1/012014.
17. Ahmad, S.B.; Irmawaty, R.; Aly, S.H.; Amiruddin, A. Performance of Fly Ash Concrete with Nickel Slag Fine Aggregate in the Marine Environment. *Civ. Eng. J.* **2022**, *8*, 2803–3814. https://doi.org/10.28991/CEJ-2022-08-12-010.
18. Sun, J.; Feng, J.; Chen, Z. Effect of Ferronickel Slag as Fine Aggregate on Properties of Concrete. *Constr. Build. Mater.* **2019**, *206*, 201–209. https://doi.org/10.1016/j.conbuildmat.2019.01.187.
19. Saha, A.K.; Majhi, S.; Sarker, P.K.; Mukherjee, A.; Siddika, A.; Aslani, F.; Zhuge, Y. Non-Destructive Prediction of Strength of Concrete Made by Lightweight Recycled Aggregates and Nickel Slag. *J. Build. Eng.* **2021**, *33*, 101614. https://doi.org/10.1016/j.jobe.2020.101614.
20. Szewczyk, P.; Kudyba, P. Effectiveness of Selected Strain and Displacement Measurement Techniques in Civil Engineering. *Buildings* **2022**, *12*, 172. https://doi.org/10.3390/buildings12020172.
21. Bhoopathy, V.; Subramanian, S.S. The Way Forward to Sustain Environmental Quality through Sustainable Sand Mining and the Use of Manufactured Sand as an Alternative to Natural Sand. *Environ. Sci. Pollut. Res.* **2022**, *29*, 30793–30801. https://doi.org/10.1007/s11356-022-19633-w.
22. Elavenil, D.S.; Bhoopathy, V. Manufactured Sand, a Solution and An Alternative to River Sand in Concrete Manufacturing. *Int. J. Civ. Eng. Res. Dev. (IJCERD)* **2013**, *3*, 7.
23. *ASTM C 192/C 192M*, Standard Practice for Making and Curing Concrete Test Specimens in the Laboratory. ASTM International: West Conshohocken, USA, 2002.
24. Pan, B.; Qian, K.; Xie, H.; Asundi, A. Two-Dimensional Digital Image Correlation for in-Plane Displacement and Strain Measurement: A Review. *Meas. Sci. Technol.* **2009**, *20*, 062001.
25. *SNI 1974*, Cara Uji Kuat Tekan Beton dengan Benda Uji Silinder. Badan Standardisasi Nasional: Jakarta, Indonesia, 2011.
26. *ASTM C 39*, Test Method for Compressive Strength of Cylindrical Concrete Specimens. ASTM International: West Conshohocken, USA, 1999.
27. Li, Z.-Q.; Chen, H.; Dong, J.; Yan, X.; Zhao, S.-R.; Zheng, Y.-H.; Liu, Y. Study of the Failure Mechanism of Mortar Rubble Using Digital Image Correlation, Acoustic Emission and Scanning Electron Microscopy. *Buildings* **2022**, *12*, 1313. https://doi.org/10.3390/buildings12091313.
28. Deltanto, A.D.; Handika, N.; Sentosa, B.O.B. *Response of Load-Displacement on Cubical Sample of Oil-Palm Shell with Fly Ash Concrete Using Digital Image Correlation System*; AIP Publishing LLC: Depok, Indonesia, 2021; p. 040007.
29. Handika, N. Multi-Cracking of Reinforced Concrete Structures: Image Correlation Analysis and Modelling. Ph.D. Thesis, INSA de Toulouse, Toulouse, France, 2017.
30. Hongsen, K.; Melhan, M.; Handika, N.; Sentosa, B.O.B. Parameterization of Oil Palm Shell Concrete on Numerical Damage Model Based on Laboratory Experiment Using Digital Image Correlation. *J. Phys.: Conf. Ser.* **2021**, *1858*, 012029. https://doi.org/10.1088/1742-6596/1858/1/012029.
31. Handika, N.; Norita, B.F.; Tjahjono, E.; Arijoeni, E. Experimental Studies on the Homogeneity and Compressive Strength Prediction of Recycled Aggregate Concrete (RAC) Using Ultrasonic Pulse Velocity (UPV). *CSID-JID* **2020**, *3*, 117. https://doi.org/10.32783/csid-jid.v3i2.111.
32. Jahami, A.; Khatib, J.; Raydan, R. Production of Low-Cost, High-Strength Concrete with Waste Glass as Fine Aggregates Replacement. *Buildings* **2022**, *12*, 2168. https://doi.org/10.3390/buildings12122168.
33. Saha, A.K.; Sarker, P.K.; Majhi, S. Effect of Elevated Temperatures on Concrete Incorporating Ferronickel Slag as Fine Aggregate. *Fire Mater.* **2019**, *43*, 8–21. https://doi.org/10.1002/fam.2664.
34. Sevim, O.; Alakara, E.H.; Guzelkucuk, S. Fresh and Hardened Properties of Cementitious Composites Incorporating Firebrick Powder from Construction and Demolition Waste. *Buildings* **2022**, *13*, 45. https://doi.org/10.3390/buildings13010045.
35. Neville, A.M.; Brooks, J.J. *Concrete Technology*, 2nd ed.; Prentice Hall: Harlow, UK, 2010; ISBN 978-0-273-73219-8.
36. Park, R.; Paulay, T. *Reinforced Concrete Structures*; J. Wiley & Sons: New York, NY, USA, 1975; ISBN 978-0-471-65917-4.
37. Belyadi, H.; Fathi, E.; Belyadi, F. Rock Mechanical Properties and in Situ Stresses. In *Hydraulic Fracturing in Unconventional Reservoirs*; Elsevier: Amsterdam, The Netherlands, 2019; pp. 215–231, ISBN 978-0-12-817665-8.